Notes on Internal Conversion Coefficients

W. R. Johnson
Department of Physics, University of Notre Dame
225 Nieuwland Science Hall, Notre Dame, IN 46556

May 16, 2017

Abstract

These notes are preparatory to studies of internal conversion coefficients based on Dirac-Fock wave functions including RPA corrections. The theory of internal conversion coefficients is reviewed and preliminary calculations are carried out using Dirac-Slater and Dirac-Fock wave functions. Results of the present calculations are compared with earlier published Dirac-Slater calculations of electric and magnetic conversion coefficients for multipolarities 1 to 4, for all subshells of the L, M and N shells of Zn, in the range of photon energies from threshold to 20 keV. (Internal conversion from the K shell of atoms with $Z \geq 2$ is forbidden in this energy range.) Comparisons with previous Dirac-Fock calculations of conversion coefficients are also carried out for multipolarities from 1 to 4 for the L shell of Zn. The present calculations, using both Dirac-Slater and Dirac-Fock wave functions, are in good agreement with previously tabulated conversion coefficients for electric multipoles, however, they are somewhat smaller than results of previous calculations for magnetic multipoles.

1 Basic Equations

In the following paragraphs, we set up the basic equations governing the internal conversion process, in which the energy $\omega = E_A - E_A$ released in a radiative nuclear transition from state Ψ_A to state Ψ_B is transferred through a virtual photon to a bound state u_a in the atom surrounding the nucleus, which makes a transition to a final electron continuum state u_b with energy $e_b = e_a + \omega$. The internal conversion coefficient is defined as the ratio of continuum electron transition rate to the radiative transition rate. There are several detailed theoretical descriptions of the internal conversion process [1–3] and several extensive tabulations of internal conversion coefficients [4–8] based on increasingly sophisticated numerical calculations. In the following note, we follow Akhiezer and Berestetskii [3], with some differences in normalization of radial functions and some extensions.

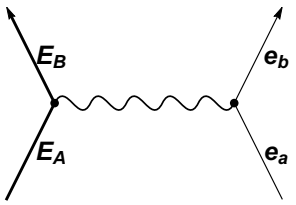

Figure 1: A nucleon in state A with energy E_A makes a transition to state B with energy E_B giving rise to a virtual photon with energy $\omega = E_A - E_B$. The virtual photon is absorbed by an electron in state a with energy e_a that makes a transition to continuum state b with energy $e_b = e_a + \omega$.

The S-matrix element for the internal conversion transition is

$$S_{fi} = -2\pi i\delta(e_a - e_b - \omega)\, U_{fi} \tag{1}$$

$$U_{fi} = \alpha \iint d^3\rho\, d^3r \frac{e^{ikR}}{R} \left[\rho_N(\boldsymbol{\rho})\rho_e(\boldsymbol{r}) - \boldsymbol{j}_N(\boldsymbol{\rho}) \cdot \boldsymbol{j}_e(\boldsymbol{r})\right], \tag{2}$$

where $\boldsymbol{R} = \boldsymbol{r} - \boldsymbol{\rho}$ and $\omega = E_A - E_B$. In the above, α designates the fine-structure constant and

$$\rho_e(\boldsymbol{r}) = u_b^\dagger(\boldsymbol{r}) u_a(\boldsymbol{r}) \qquad \boldsymbol{j}_e(\boldsymbol{r}) = u_b^\dagger(\boldsymbol{r})\boldsymbol{\alpha} u_a(\boldsymbol{r}) \tag{3}$$

$$\rho_N(\boldsymbol{r}) = \Psi_B^\dagger(\boldsymbol{\rho})\Psi_A(\boldsymbol{\rho}) \qquad \boldsymbol{j}_N(\boldsymbol{\rho}) = \Psi_B^\dagger(\boldsymbol{\rho})\boldsymbol{\alpha}\Psi_A(\boldsymbol{\rho}). \tag{4}$$

The transition rate for electrons into solid angle $d\Omega_p$ is

$$dw = \frac{p_b e_b}{(2\pi c)^2 \hbar^4}\, |U_{fi}|^2 d\Omega_p, \tag{5}$$

Where p_b and e_b are the momentum and energy of the continuum electron in state b. In numerical calculations, we make a point-nucleus approximation which implies: $\rho < r$. Consequences of this approximation are discussed, for example, in Ref. [2, 9]. With this ordering of r and ρ in mind, we expand the retarded potential as

$$\frac{e^{ikR}}{R} = 4\pi ik \sum_{LM} j_L(k\rho)\, h_L^{(1)}(kr)\, Y_{LM}^*(\hat{\rho})\, Y_{LM}(\hat{r}) \tag{6}$$

$$= 4\pi ik \sum_{LM} \Big(j_L(k\rho)\, Y_{LM}^*(\hat{\rho})\Big) \Big(h_L^{(1)}(kr)\, Y_{LM}(\hat{r})\Big), \tag{7}$$

where $j_L(x)$ and $h_L^{(1)}(x)$ are spherical Bessel and Hankel functions, respectively. Note: $h_L^{(1)}(x) = j_L(x) + iy_L(x)$.

We define

$$\phi(k\rho) = j_L(k\rho) Y_{LM}(\hat{\rho}) \tag{8}$$

$$\Phi(kr) = h_L^{(1)}(kr) Y_{LM}(\hat{r}) \tag{9}$$

to find

$$\frac{e^{ikR}}{R}\rho_N(\boldsymbol{\rho})\rho_e(\boldsymbol{r}) = 4\pi ik\sum_{LM}\Big(\phi^*(k\rho)\rho_N(\boldsymbol{\rho})\Big)\Big(\rho_e(\boldsymbol{r})\Phi(kr)\Big) \tag{10}$$

We may expand the nuclear current term times the retarded potential in terms of vector spherical harmonics as

$$\frac{e^{ikR}}{R}\ \boldsymbol{j}_N(\boldsymbol{\rho}) = \sum_{JLM} C_{JLM}(r,\boldsymbol{\rho})\boldsymbol{Y}_{JLM}(\hat{r}) \tag{11}$$

with

$$\begin{aligned} C_{JLM} =&\ \int d\Omega \boldsymbol{Y}^\dagger_{JLM}(\hat{r})\cdot\left(\frac{e^{ikR}}{R}\ \boldsymbol{j}_N(\boldsymbol{\rho})\right) &(12)\\ =&\ 4\pi ik\sum_{lm}\left(\int d\Omega_r \boldsymbol{Y}^\dagger_{JLM}(\hat{r})Y_{lm}(\hat{r})\right)Y^*_{lm}(\hat{\rho})\cdot\boldsymbol{j}_N(\boldsymbol{\rho})\, j_l(k\rho)\, h^{(1)}_l(kr)\\ =&\ 4\pi ik\,\boldsymbol{Y}^\dagger_{JLM}(\hat{\rho})\cdot\boldsymbol{j}_N(\boldsymbol{\rho})\, j_L(k\rho)\, h^{(1)}_L(kr). &(13)\end{aligned}$$

It follows that

$$\boldsymbol{j}_e(\boldsymbol{r})\cdot\boldsymbol{j}_N(\rho)\ \frac{e^{ikR}}{R} = 4\pi ik\sum_{JLM}\Big(\boldsymbol{a}^\dagger_{JLM}(\boldsymbol{\rho})\cdot\boldsymbol{j}_N(\rho)\Big)\Big(\boldsymbol{j}_e(\boldsymbol{r})\cdot\boldsymbol{A}_{JLM}(\boldsymbol{r})\Big), \tag{14}$$

with

$$\begin{aligned} \boldsymbol{a}_{JLM}(\boldsymbol{\rho}) =&\ j_L(k\rho)\boldsymbol{Y}_{JLM}(\hat{\rho}) &(15)\\ \boldsymbol{A}_{JLM}(\boldsymbol{r}) =&\ h^{(1)}_L(kr)\boldsymbol{Y}_{JLM}(\hat{r}). &(16)\end{aligned}$$

As an alternative, we can expand the currents in terms of the vector spherical harmonics functions $\boldsymbol{Y}^{(\lambda)}_{JM}$, leading to the following relations:

$$\begin{aligned} \boldsymbol{a}^{(0)}_{JM} =&\ j_J(k\rho)Y_{JJM}(\hat{\rho}) &(17)\\ \boldsymbol{a}^{(1)}_{JM} =&\ \sqrt{\frac{J+1}{2J+1}}j_{J-1}(k\rho)\boldsymbol{Y}_{JJ-1M} - \sqrt{\frac{J}{2J+1}}j_{J+1}(k\rho)\boldsymbol{Y}_{JJ+1M} &(18)\\ \boldsymbol{a}^{(-1)}_{JM} =&\ \sqrt{\frac{J}{2J+1}}j_{J-1}(k\rho)\boldsymbol{Y}_{JJ-1M} + \sqrt{\frac{J+1}{2J+1}}j_{J+1}(k\rho)\boldsymbol{Y}_{JJ+1M}, &(19)\end{aligned}$$

and similar expressions for $\boldsymbol{A}^{(\lambda)}_{JM}(\boldsymbol{r})$ with $j_L(k\rho)\to h^{(1)}_L(kr)$.

With the above in mind, we find

$$\begin{aligned} U_{fi} = 4\pi ike^2\sum_{JM}\iint d^3r d^3\rho\Big[&\Big(\phi^*_{JM}(\boldsymbol{\rho})\rho_N(\boldsymbol{\rho})\Big)\Big(\rho_e(\boldsymbol{r})\Phi_{JM}(\boldsymbol{r})\Big)\\ &-\sum_{\lambda=-1}^{1}\Big(\boldsymbol{a}^{(\lambda)\dagger}_{JM}(\boldsymbol{\rho})\cdot\boldsymbol{j}_N(\boldsymbol{\rho})\Big)\Big(\boldsymbol{j}_e(\boldsymbol{r})\cdot\boldsymbol{A}^{(\lambda)}_{JM}(\boldsymbol{r})\Big)\Big] \end{aligned} \tag{20}$$

At this point, it is useful to recall the following identity that follows from guage invariance:

$$\int d^3\rho\ \phi^*_{JM}(\boldsymbol{\rho})\rho_N(\boldsymbol{\rho}) = i\int d^3\rho\ \boldsymbol{a}^{(-1)\dagger}_{JM}(\boldsymbol{\rho})\cdot\boldsymbol{j}_N(\boldsymbol{\rho}). \tag{21}$$

In the expression for $\boldsymbol{a}^{(-1)}_{JM}(\boldsymbol{\rho})$, we note that terms containing $j_{J+1}(k\rho)$ are smaller than those containing $j_{J-1}(k\rho)$ by order $(k\rho)^2$ and can therefore be ignored, leading to

$$\boldsymbol{a}^{(-1)}_{JM} = \sqrt{\frac{J}{J+1}}\ \boldsymbol{a}^{(1)}_{JM}. \tag{22}$$

Therefore,

$$\int d^3\rho\ \phi^*_{JM}(\boldsymbol{\rho})\rho_N(\boldsymbol{\rho}) = i\sqrt{\frac{J}{J+1}}\ \int d^3\rho\ \boldsymbol{a}^{(1)\dagger}_{JM}(\boldsymbol{\rho})\cdot\boldsymbol{j}_N(\boldsymbol{\rho}). \tag{23}$$

With the aid of Eqs. (21,22), we can eliminate the scalar potential terms and express the integrand of U_{fi} in terms of the nuclear electric $\boldsymbol{a}^{(1)\dagger}_{\boldsymbol{JM}}$ and magnetic $\boldsymbol{a}^{(0)\dagger}_{\boldsymbol{JM}}$ multipole operators only:

$$U_{fi} = 4\pi ike^2\sum_{JM}\sum_{\lambda=0}^{1}\int T^{(\lambda)}_{JM}(\boldsymbol{\rho})\,d^3\rho\int B^{(\lambda)}_{JM}(\boldsymbol{r})\,d^3r, \tag{24}$$

where

$$T^{(\lambda)}_{JM} = \left(\boldsymbol{a}^{(\lambda)\dagger}_{\boldsymbol{JM}}\cdot\boldsymbol{j}_N(\boldsymbol{\rho})\right) \tag{25}$$

and

$$B^{(0)}_{JM} = -\boldsymbol{j}_e\cdot\boldsymbol{A}^{(0)}_{JM} = -\boldsymbol{j}_e\cdot\boldsymbol{A}_{JJM} \tag{26}$$

$$B^{(1)}_{JM} = -\boldsymbol{j}_e\cdot\left(\boldsymbol{A}^{(1)}_{JM} + \sqrt{\frac{J}{J+1}}\boldsymbol{A}^{(-1)}_{JM}\right) + i\sqrt{\frac{J}{J+1}}\,\rho_e\Phi_{JM} \tag{27}$$

$$= -\sqrt{\frac{2J+1}{J+1}}\ \boldsymbol{j}_e\cdot\boldsymbol{A}_{JJ-1M} + i\sqrt{\frac{J}{J+1}}\,\rho_e\Phi_{JM}, \tag{28}$$

where

$$\boldsymbol{A}_{JJM}(\boldsymbol{r}) = h^{(1)}_J(kr)\,\boldsymbol{Y}_{JJM}(\hat{r}) \tag{29}$$

$$\boldsymbol{A}_{JJ-1M}(\boldsymbol{r}) = h^{(1)}_{J-1}(kr)\,\boldsymbol{Y}_{JJ-1M}(\hat{r}). \tag{30}$$

and

$$\Phi_{JM}(\boldsymbol{r}) = h^{(1)}_J(kr)Y_{JM}(\hat{r}). \tag{31}$$

We introduce the T matrices for a nuclear radiative transitions

$$\left\langle T^{(\lambda)}_{JM}\right\rangle = \int d^3\rho\ \boldsymbol{a}^{(\lambda)\dagger}_{\boldsymbol{JM}}(\boldsymbol{\rho})\cdot\boldsymbol{j}_N(\boldsymbol{\rho}). \tag{32}$$

and the associated atomic matrices

$$\left\langle B^{(\lambda)}_{JM} \right\rangle = \int d^3r \; B^{(\lambda)}_{JM}(\boldsymbol{r}) \tag{33}$$

It should be noted that $\left\langle T^{(\lambda)}_{JM} \right\rangle$ is precisely the multipole transition operator used in [10] to treat atomic multipole transitions. The corresponding nuclear radiative transition rate is

$$\left(w^{(\lambda)}_{JM}\right)_{\rm rad} = 8\pi\alpha\omega \left|\left\langle T^{(\lambda)}_{JM} \right\rangle\right|^2 \tag{34}$$

For a nuclear internal conversion transition with a specific multipolarity, the differential transition rate

$$d\left(w^{(\lambda)}_{JM}\right)_{\rm IC} = \frac{4\alpha^2 p_b e_b \omega^2}{(\hbar c)^2} \left|\left\langle T^{(\lambda)}_{JM} \right\rangle\right|^2 \left|\left\langle B^{(\lambda)}_{JM} \right\rangle\right|^2 d\Omega_p, \tag{35}$$

$$= \frac{\alpha}{2\pi} \frac{p_b e_b \omega}{(\hbar c)^2} \left(w^{(\lambda)}_{JM}\right)_{\rm rad} \left|\left\langle B^{(\lambda)}_{JM} \right\rangle\right|^2 d\Omega_p \tag{36}$$

The internal conversion coefficient $\beta^{(\lambda)}_J$ is defined as the ratio of the ICC rate to the radiative transition rate. Thus, summing over a complete electron subshell m_a and over outgoing electron spins σ, we find

$$\beta^{(\lambda)}_J = \frac{\left(w^{(\lambda)}_{JM}\right)_{\rm IC}}{\left(w^{(\lambda)}_{JM}\right)_{\rm rad}} = \frac{\alpha}{2\pi} \frac{p_b e_b \omega}{(\hbar c)^2} \sum_{m_a \sigma} \int \left|\left\langle B^{(\lambda)}_{JM} \right\rangle\right|^2 d\Omega_p \tag{37}$$

Note that $\beta^{(\lambda)}_J$ is independent of M, which is determined by the nuclear transition.

We make use of the expansions

$$u^\dagger_b(\boldsymbol{r})\boldsymbol{\alpha} u_a(\boldsymbol{r}) = \sum_{JLM} D_{JLM}(r) \boldsymbol{Y}_{JLM}(\hat{r}) \tag{38}$$

$$u^\dagger_b(\boldsymbol{r}) u_a(\boldsymbol{r}) = \sum_{JM} D_{JM}(r) Y_{JM}(\hat{r}) \tag{39}$$

to rewrite the angular integrals

$$\int d\Omega \, u^\dagger_b \, \boldsymbol{\alpha} \cdot \boldsymbol{Y}^*_{JLM} \, u_a = -\frac{i}{r^2} D_{JLM}(r), \tag{40}$$

$$\int d\Omega \, u^\dagger_b \, Y^*_{JM} \, u_a = \frac{1}{r^2} D_{JM}(r), \tag{41}$$

where

$$D_{JJ-1M} = \langle \kappa_a m_a | Y_{JM} | \kappa_b M_b \rangle \sqrt{\frac{J}{2J+1}} P_{ab}(r) \tag{42}$$

$$D_{JJM} = \langle \kappa_a m_a | Y_{JM} | \kappa_b M_b \rangle \sqrt{\frac{1}{J(J+1)}} Q_{ab} \tag{43}$$

$$D_{JM} = \langle \kappa_a m_a | Y_{JM} | \kappa_b M_b \rangle \, S_{ab} \tag{44}$$

with

$$P_{ab}(r) = U_{ab}(r) + \frac{\kappa_b - \kappa_a}{J} V_{ab}(r) \tag{45}$$

$$Q_{ab}(r) = (\kappa_a + \kappa_b) V_{ab} \tag{46}$$

$$U_{ab}(r) = G_a(r)F_b(r) - F_a(r)G_b(r) \tag{47}$$

$$V_{ab}(r) = G_a(r)F_b(r) + F_a(r)G_b(r) \tag{48}$$

$$S_{ab}(r) = G_a(r)G_b(r) + F_a(r)F_b(r) \tag{49}$$

It follows that

$$\left\langle B^{(1)}_{JM} \right\rangle = i\sqrt{\frac{2J+1}{4\pi J(J+1)}} \langle \kappa_a m_a | C_{JM} | \kappa_b m_b \rangle R^{(1)}_J \tag{50}$$

$$\left\langle B^{(0)}_{JM} \right\rangle = i\sqrt{\frac{2J+1}{4\pi J(J+1)}} \langle \kappa_a m_a | C_{JM} | \kappa_b m_b \rangle R^{(0)}_J, \tag{51}$$

where $R^{(\lambda)}_J$ are radial integrals

$$R^{(1)}_J = \int_0^\infty dr\ J \left[P_{ab}(r)\ h^{(1)}_{J-1}(kr) + S_{ab}(r)\ h^{(1)}_J(kr) \right] \tag{52}$$

$$R^{(0)}_J = \int_0^\infty dr\ Q_{ab}(r)\ h^{(1)}_J(kr). \tag{53}$$

The final state wave function is a continuum function that behaves asymptotically as a plane wave with momentum $\boldsymbol{p}$ and spin σ plus a spherical incoming wave. This fact can be implemented in the previous formulas by the replacement

$$\begin{pmatrix} G_b(r) \\ F_b(r) \end{pmatrix} \to 4\pi \sum_{\kappa_b, m_b} \left(\Omega^\dagger_{\kappa_b m_b}(\hat{p}) \chi_\sigma \right) i^{l_b - 1} e^{-i\delta_b} \begin{pmatrix} G_b(r) \\ F_b(r) \end{pmatrix}. \tag{54}$$

When $\left\langle B^{(\lambda)}_{JM} \right\rangle$ is squared, summed over a complete electron subshell m_a and outgoing electron spins σ and integrated over angles of $\boldsymbol{p}$, we obtain the following expression for the ICC for electrons emitted from subshell a:

$$\beta^{(\lambda)}_J = \frac{2\alpha p_b e_b \omega}{(\hbar c)^2} \sum_{\kappa_b} \frac{|\langle \kappa_a \| C_J \| \kappa_b \rangle|^2}{J(J+1)} \left| R^{(\lambda)}_J \right|^2. \tag{55}$$

In the above expression, the continuum wave function is a box-normalized plane wave asymptotically. To normalize the continuum on the energy scale, we must multiply the $G_b(r)$ and $F_b(r)$ by the factor

$$\sqrt{\frac{2e_b p_b}{\pi c^2}}$$

With continuum wave functions normalized on the energy scale and expressed in atomic units, we obtain

$$\beta^{(\lambda)}_J = \pi\alpha\omega \sum_{\kappa_b} \frac{|\langle \kappa_a \| C_J \| \kappa_b \rangle|^2}{J(J+1)} \left| R^{(\lambda)}_J \right|^2. \tag{56}$$

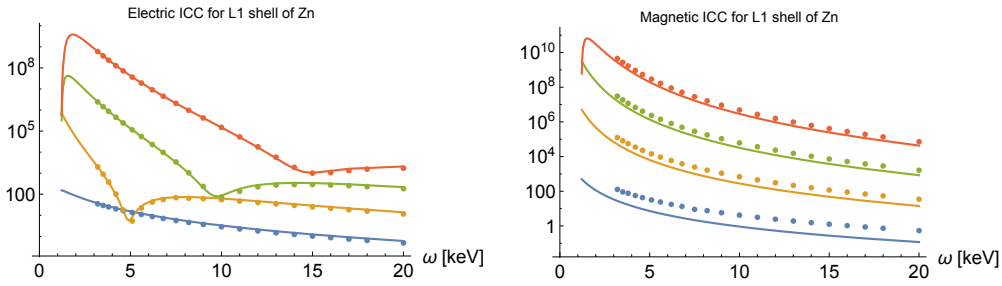

Figure 2: Comparison of electric ICC's (left panel) and magnetic ICC's (right panel) for the L_1 subshell of Zn obtained using the present Dirac-Slater wave functions (solid lines) with ICC's from Ref. [7] (colored dots). The L_1 threshold is at $\omega = 1193.6\ eV$.

The above agrees precisely with the expression for the ICC given by Rösel et al. [7].

Example: K-shell ICC

Electric multipole transitions from the $1s_{1/2}$ state ($\kappa_a = -1$) lead to final states with angular momentum $J \pm 1/2$ and parity $(-1)^J$. These states are $(p_{1/2},\ p_{3/2})$, $(d_{3/2},\ d_{5/2})$ and $(f_{5/2},\ f_{7/2})$, for $J = 1,\ 2$ and 3, respectively. Magnetic dipole transitions, on the other hand, lead to final states with angular momentum $J \pm 1/2$ and parity $(-1)^{J+1}$. These states are $(s_{1/2},\ d_{3/2})$, $(p_{3/2},\ f_{5/2})$ and $(d_{5/2},\ g_{7/2})$, for $J = 1,\ 2$ and 3, respectively. The selection rules can be rephrased in terms of κ_b as $\kappa_b = J,\ -J-1$ for $\lambda = 1$ and $\kappa_b = -J,\ J+1$ for $\lambda = 0$.

We find:

$$\beta_J^{(0)}(\kappa_a = -1) = \frac{2\pi\omega}{(2J+1)J(J+1)} \left\{ J \left| R_J^{(0)}(\kappa_b = -J) \right|^2 + (J+1) \left| R_J^{(0)}(\kappa_b = J+1) \right|^2 \right\} \quad (57)$$

$$\beta_J^{(1)}(\kappa_a = -1) = \frac{2\pi\omega}{(2J+1)J(J+1)} \left\{ J \left| R_J^{(1)}(\kappa_b = J) \right|^2 + (J+1) \left| R_J^{(1)}(\kappa_b = -(J+1)) \right|^2 \right\} \quad (58)$$

2 Comparison with Dirac-Slater calculations

As a preliminary study, we examine the ICC's for subshells of Zn (Z=30) using Dirac-Slater (DS) bound-state and continuum wave functions. In Table 1,

Table 1: Dirac-Slater (DS) and Dirac-Fock (DF) eigenvalues for subshells of zinc Z=30 are compared with edge energies (NIST) [11] and inner-shell binding energies (B&B) Bearden and Burr [12]. The entry under B&B for the N_1 sublevel is the $4s$ removal energy from Ref. [13].

Shell	DS	DF	NIST	B&B
K	9621.6	9734.7	9658.6	9659.0
L_1	1183.6	1233.9	1193.6	1196.2
L_2	1049.7	1081.4	1042.8	1044.9
L_3	1025.1	1057.2	1019.7	1021.8
M_1	136.6	157.8	135.9	139.8
M_2	92.9	107.7	86.6	91.4
M_3	89.7	104.4	86.6	88.6
M_4	15.9	21.0	8.1	10.2
M_5	15.5	20.5	8.1	10.1
N_1	7.6	8.1		9.4

we compare the Dirac-Slater eigenvalues with Dirac-Fock eigenvalues and with experimental inner-shell binding energies from Refs. [11, 12]. The Dirac-Slater eigenvalues are seen to be in somewhat better agreement with experimental removal energies than the corresponding Dirac-Fock (DF) eigenvalues.

In Fig. 2, we compare our calculations of electric and magnetic ICC's for the L_1 subshell of Zn with the calculations from Ref. [7], which were also carried out using Dirac-Slater wave functions. In both calculations, experimental energies rather than DS eigenvalues are use to determine the momentum p_b of the continuum electron. In these figures, the solid lines are from the present calculation, while the colored dots are from Rösel et al. [7], The multipolarity of the ICC calculations ranges from 1 to 4, the lower blue curves refer to transitions having multipolarity $L = 1$ whereas the upper red curve refers to those with multipolariy $L = 4$. Electric ICC's for the L_1 subshell predicted by the present code agree well with those from [7] throughout the range of the plot. The agreement is poorer, however, for the magnetic multipole transitions.

Internal conversion coefficients for the L_2 and L_3 subshells of Zn are presented in Fig. 3, where they are compared with values tabulated by Hager and Seltzer [6] shown by colored swatches and by Rösel et al. [7] shown by colored dots. Again, there is good agreement of electric ICCs for both L_2 and L_3 subshells of Zn and somewhat poorer agreement for magnetic ICC's between the present values and those from Refs. [6, 7].

In Fig. 6 we compare results from the present calculation for each of the five subshells of the ($n = 3$) subshell of Zn with values from Ref. [7]. The respective thresholds are taken from the final column of Table 1 [12].

Finally, in Fig.5, we compare the present values of electric and magnetic ICC's for the outermost N_1 shell of Zn in the range 1.5-20 keV with data from

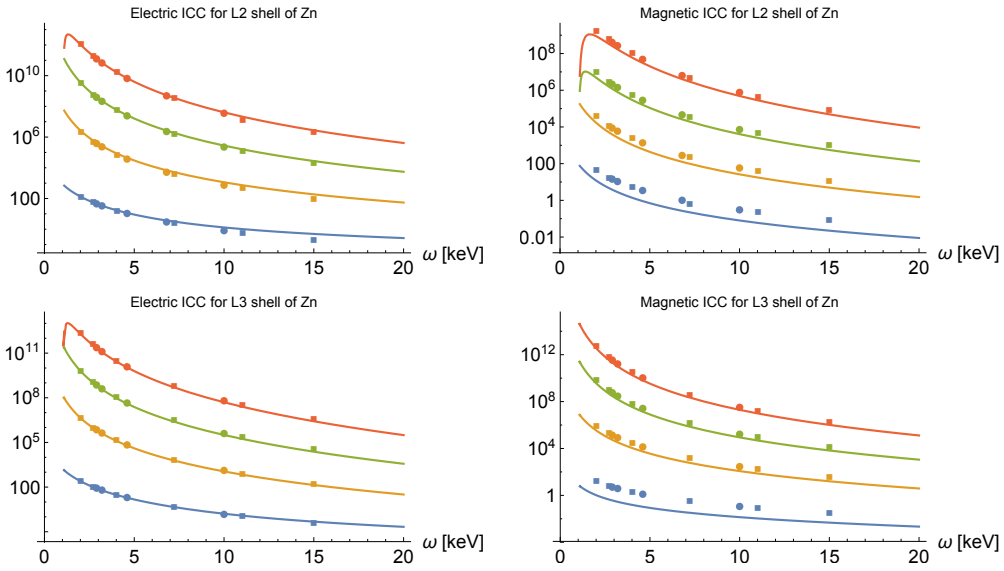

Figure 3: Electric and Magnetic ICC's for the L_2 and L_3 subshells of Zn from the present calculation, shown by the solid lines, are compared with values from Ref. [6] shown by colored swatches and from Ref. [7] shown by colored dots.

[7]. Once again, the agreement for electric ICC's is better than for magnetic ICC's. Differences in the numerical treatment of the region inside the nucleus may be responsible for the differences found in the magnetic ICC's.

3 Comparison with Dirac-Fock calculations

In the previous section we compared conversion coefficients from the present study for the example of Zn with calculations by Rösel et al. and by Hager and Seltzer that were carried out in the second half of the previous century using Dirac-Slater wave functions and experimental binding energies. Here, we compare our calculations for the L-shell of Zn with the conversion coefficients that were evaluated using Dirac-Fock bound state and continuum wave functions together with experimental binding energies calculations by Band et al. [8] that were carried out at the beginning of this century and also used Dirac-Fock wave functions and experimental binding energies. Again there is good agreement between our calculations and those of [8] for electric multipole transitions and somewhat poorer agreement for magnetic multipole transitions.

References

[1] M. E. Rose, *Multipole Fields* (Wiley, 1965).

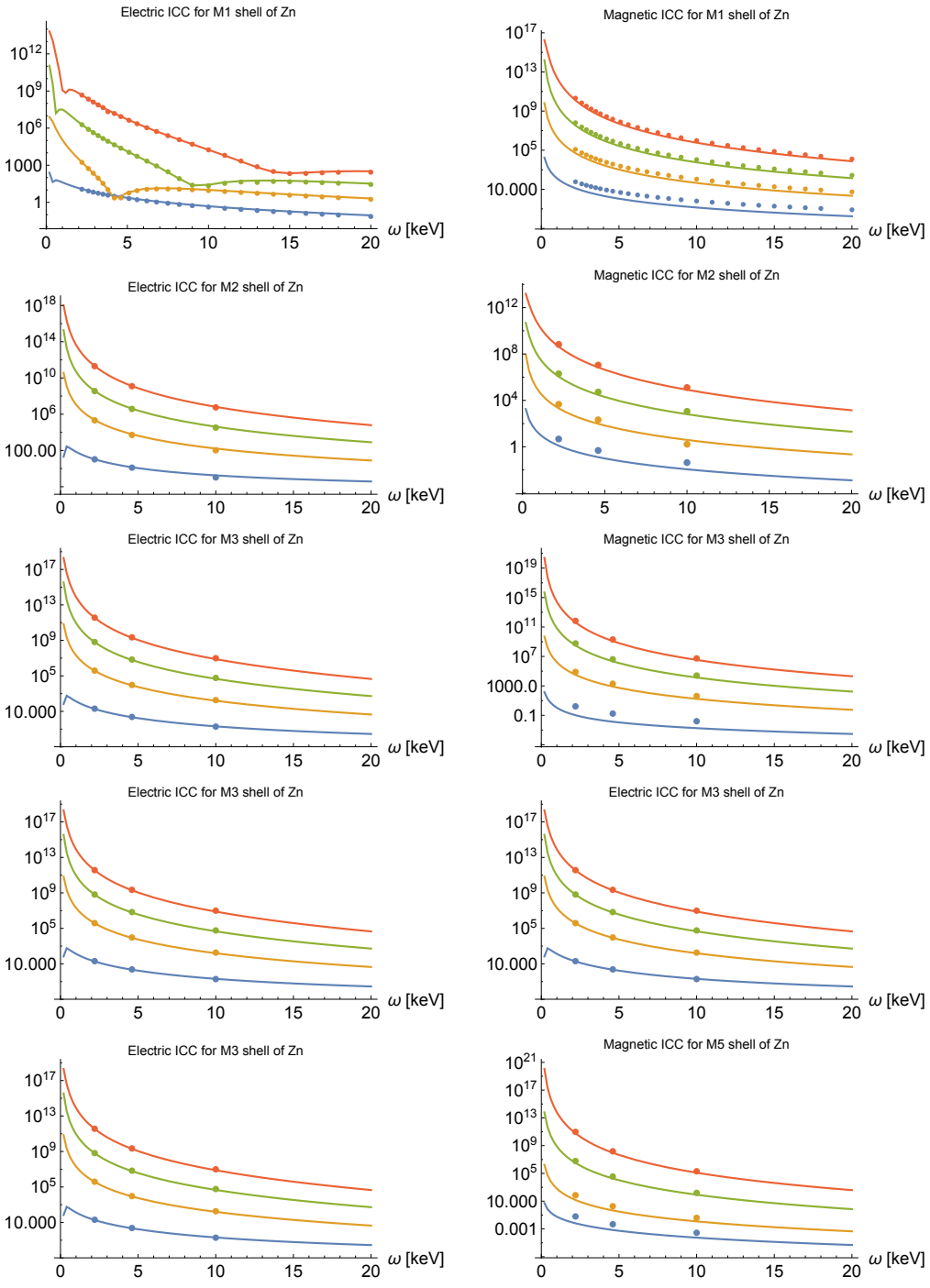

Figure 4: Electric and Magnetic ICC's for subshells of the M-shell (n=3) of Zn from the present calculation, shown by the solid lines, are compared with values from Ref. [7] shown by colored dots.

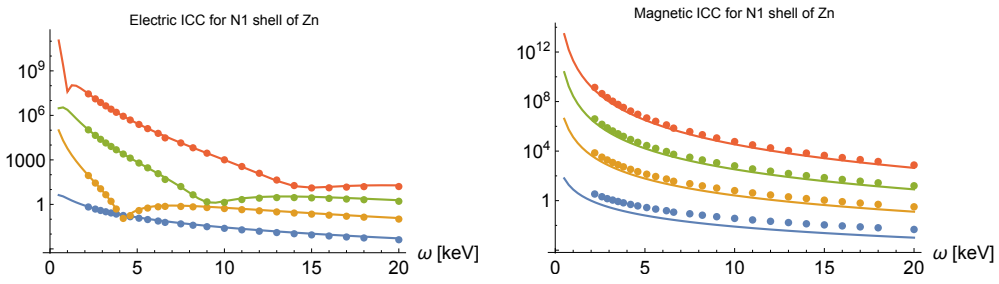

Figure 5: Electric and magnetic ICC's from the present calculation (solid lines) are compared with those from Ref. [7] (dots). The N_1 threshold is $\omega = 9.4\ eV$.

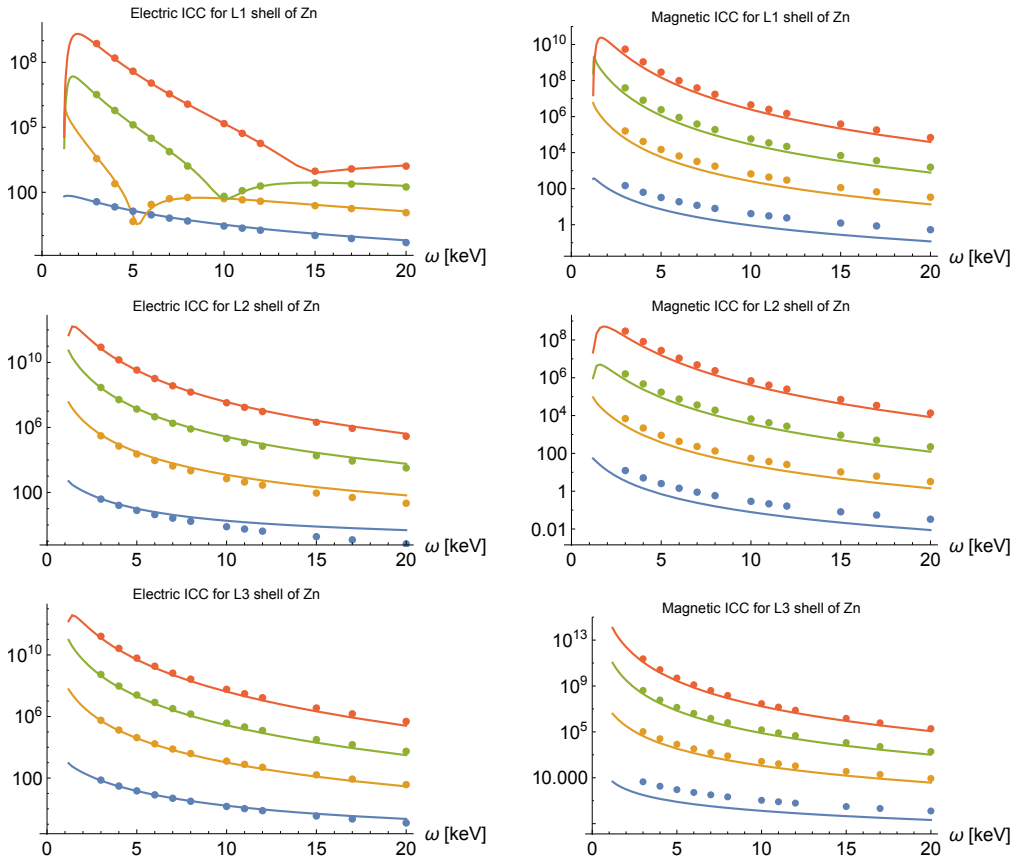

Figure 6: Electric and Magnetic ICC's for subshells of the L-shell (n=2) of Zn from the present Dirac-Fock calculation, shown by the solid lines, are compared with values from Ref. [8] shown by colored dots.

[2] E. L. Church and J. Weneser, Ann. Rev. Nucl. Sci. **10**, 193 (1960).

[3] A. I. Akhiezer and V. B. Berestetskii, *Quantum Electrodynamics* (Interscience, 1965), chap. VI, §40.

[4] M. E. Rose, *Internal Conversion Coefficients* (North- Holland, 1958).

[5] L. A. Sliv and . M. Band, in *Alpha, Beta and Gamma-Ray Spectroscopy*, edited by K. Siegbahn (North-Holland Publishing Comapny, Amsterdam, 1966), vol. 2, chap. XVIII (C), p. 1639.

[6] R. S. Hager and E. C. Seltzer, Nucl. Data Sheets **A4**, 1 (1968).

[7] F. Rösel, H. M. Fries, K. Alder, and H. C. Pauli, At Data Nucl Data Tables **21**, 91 (1978).

[8] I. M. Band, M. B. Trzhaskovskaya, C. W.Nestor, Jr., P. O. Tikkanen, and S. Raman, At Data Nucl Data Tables **81**, 1 (2002).

[9] T. R. Gerholm and R. G. Pettersson, in *Alpha, Beta and Gamma-Ray Spectroscopy*, edited by K. Siegbahn (North-Holland Publishing Comapny, Amsterdam, 1966), vol. 2, chap. XVIII (C), pp. 981–995.

[10] W. R. Johnson, *Atomic Structure Theory* (Springer, 2010).

[11] C. Chantler, K. Olsen, R. Dragoset, J. Chang, A. Kishore, S. Kotochigova, and D. Zucker, *X-Ray Form Factor, Attenuation and Scattering Tables (Version 2.1)*, `http://physics.nist.gov/ffast [11/15/2016]` (2005).

[12] J. A. Bearden and A. F. Burr, Rev. Mod. Phys. **39**, 125 (1967).

[13] A. Kramida, Yu. Ralchenko, J. Reader, and NIST ASD Team, NIST Atomic Spectra Database (ver. 5.3), [Online]. Available: `http://physics.nist.gov/asd` [07/01/2017]. (2015).